Supporting Information: Determining Local Magnetic Susceptibility Tensors in Paramagnetic Lanthanide Crystalline Powders from Solid-State NMR Chemical Shift Anisotropies

Ridvan Ince,[†] Abdelatif Doudouh,[†] Nicolas Claiser,[†] Laurent Le Pollès,[‡] Thierry Guizouarn,[¶] Éric Furet,[‡] and Gwendal Kervern[*,†]

[†]*Université de Lorraine, UMR 7036 (UL-CNRS) CRM2, BP 70239 Boulevard des Aiguillettes, F 54506 Vandœuvre-lès-Nancy, France.*

[‡]*ENSCR, UMR 6226 (UL-CNRS) École Nationale Supérieure de Chimie de Rennes, Campus de Beaulieu - Bâtiment 10B, F 35042 Rennes Cedex, France.*

[¶]*ISCR, UMR 6226 (UL-CNRS) Université de Rennes 1, Campus de Beaulieu - Bâtiment 10B, F 35042 Rennes Cedex, France.*

E-mail: gwendal.kervern@univ-lorraine.fr

Protocol for crystal growth of $[Ln_2(C_2O_4)_3]$, 9.5 H_2O

We synthesize different lanthanides of this series, such as the lanthanum, cerium, praseodymium and the neodymium oxalates. To obtain the oxalate complexes, we start with a salt of lanthanide chloride $LnCl_3$ with Ln = La, Ce, Pr and Nd and oxalic acid $H_2C_2O_4$.

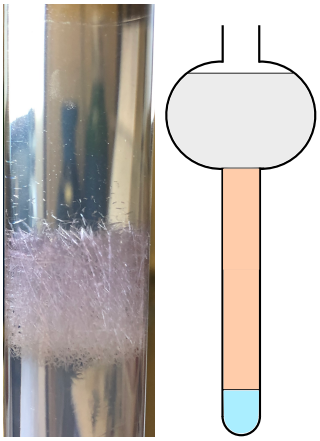

Figure S1: Setup for diffusion of lanthanide chloride salt versus oxalic acid in an agarose gel.

Our first observations from crystalization protocols based on reference[S1] showed that the higher the temperature and the lower the concentration of oxalic acid, the longer the crystaline needles were. In order to reduce as much as possible the oxalic acid concentration, a specific laboratory glassware – a test tube with a round-bottom flask welded at the top of the test tube – was made. The lanthanide chloride was set at the bottom of test tube with 5 mL of hot agarose (1% in weight). After solidification of the agarose-salt mixture, we filled the test tube to the top with agarose (1% weight). The round bottom flask was then filled with the as-dilute-as-possible oxalic acid solution. We put this glassware into the heat chamber at 50°C (higher temperature would end up with the destruction of the gel phase because of Maillard reaction). And after 2 to 3 weeks we obtained a few hundred of mg of long needles (ca 1 cm × 2 mm × 100 μm) on which diffraction experiments were performed.

Calibration of NMR experiments

Temperature calibration

Temperature calibration was performed thanks to a sample of lead nitrate that was spun at various MAS speed under controlled temperature air-flow. We used the work of Guan and Stark[S2] to measure the temperature within the rotor. After calibrating ^{207}Pb chemical shift

at low spinning speed and no temperature regulation[1], we measured the ^{207}Pb chemical shift at various regulated temperatures and spinnning speeds. We used the value of -0.749 ppm/K in Guan's paper to estimate the temperature within the rotor by comparing the shift to the reference at low-spinning speed and no regulation.

Chemical shift calibration

Chemical shifts where calibrated prior to all experiments with a standard sample of adamantane.

Short, Highpower Adiabatic Pulse (SHAP) calibration

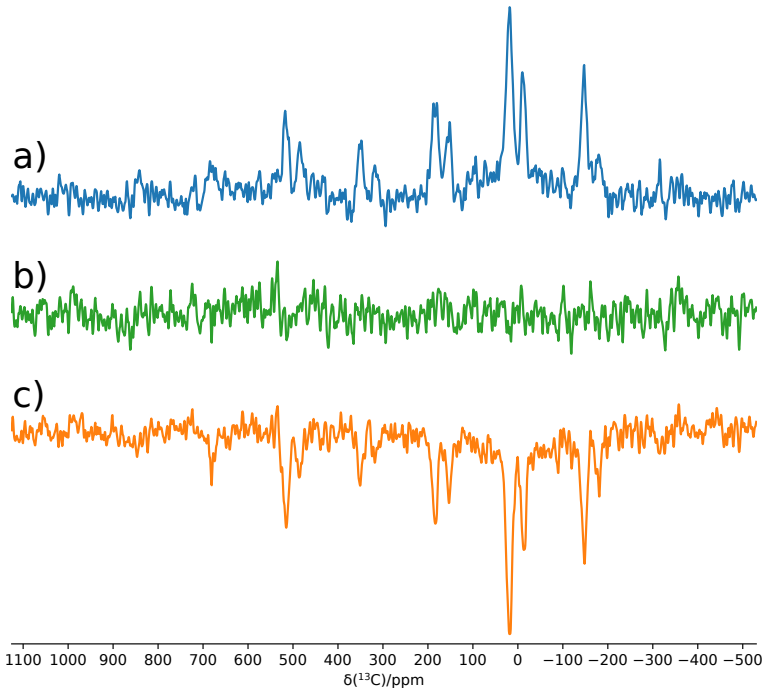

Figure S2: Experimental verification of SHAP efficiency. In a) direct acquisition of ^{13}C spectrum of $[Pr_2(C_2O_4)_3]$, 9.5 H_2O under 12.5 kHz MAS. In c), inversion recovery performed on the same sample and under the same conditions, with the inversion pulse being a TanhTan pulse of 100 μs, sweeping over a 1 MHz bandwidth under 80 kHz RF power. The spectrum presented in b) is the sum of spectra a) and c).

[1]since our CP-MAS probe has two thermocouples, one for the input air-flow and one for the output, we could verify that both thermocouples gave the same temperature reading upon calibration measurements

Since NMR spectra acquisition on the lanthanide oxalate series spans 200 kHz, the dwell time is shorter than the minimum ringdown delay imposed by Bruker software (DE parameter in Bruker systems cannot be shorter than 6.5 μs). In order not to miss the first points of the FID, one must implement a rotor-synchronized spin-echo to allow for pulse ringdown.

Being confronted with large spectral width in paramagnetic systems, the regular hard pulse inversion is not be enough to invert the full sideband patterns that span over 150 kHz in the case of praseodymium and neodymium complexes. For instance, given the RF power available with our 4 mm triple resonance probe, a regular 180° hard pulse lasts 6.12 μs, and its Fourier transform has a spectral width (90% inversion or better) of about 40 kHz.

In order to respond to this issue, we chose to use Short Highpower Adiabatic Pulses (SHAP[S3]) in a rotor-synchronized double echo. In all the experiments presented in this work, a TanhTan pulse of 100 μs, sweeping over a 1 MHz bandwidth under 80 kHz RF power was used for the rotor-synchronized double echo.

We chose this pulse design after estimating the efficiency and bandwidth thanks to the criteria proposed in Kervern's paper, and verifying experimentally the efficiency of the inversion as can be seen in figure S2.

Probe response assessment

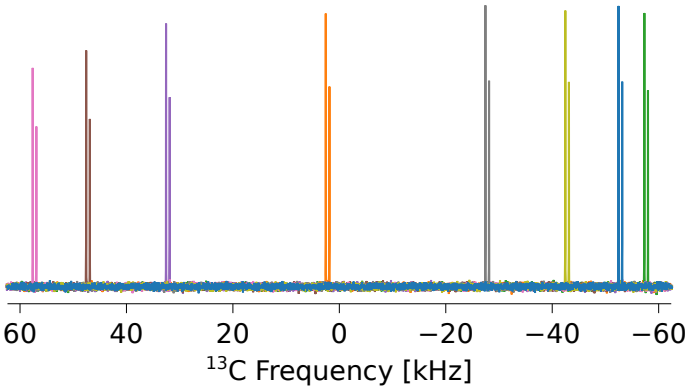

Figure S3: Direct acquisition at various ^{13}C offsets of adamantane MAS spectra under spinal 64 proton decoupling.

The probe response was tested with adamantane under direct acquisition with ^{1}H heteronuclear decoupling and variable ^{13}C offsets. The results are presented in figure S3.

This figure shows that there is a small loss of intensity on the edge of the 125 kHz acquisition window but given the fact that it is less than 10% and that it concerns the high frequency range of our spectra where the sideband intensities are the lowest, we estimated that it cannot affect our measurements significantly.

Experimental measurement and fitting of the diamagnetic CSA

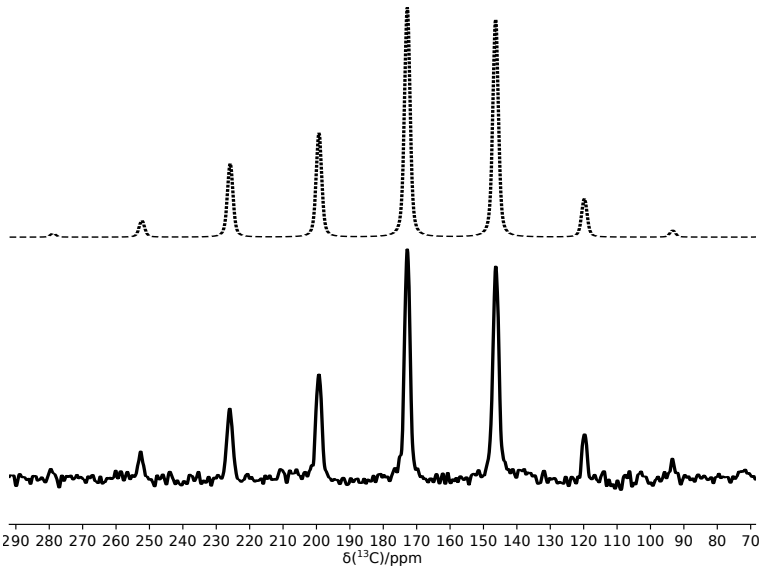

Figure S4: Fitting of the CSA tensor of the lanthanum oxalate complex. The experimental spectrum (bottom, plain) was acquired under direct acquisition at 7.05 T under 2 kHz MAS and 100 kHz spinal 64 heteronuclear decoupling, and the fitting (top, dotted) was performed by the ssNake software.

In order to consolidate the results brought by DFT for the diamagnetic contribution to the CSA, we measured the CSA tensor in the isostructural lanthanide oxalate. We acquired a low speed MAS spectrum that we processed with the DMFit software[S4]. We used the fitting capacities of this software to extract the chemical shift tensor parameters and its error:

– $\delta_{iso} = 173.2 \pm 0.02\,\text{ppm}$

– $\delta = 71.9 \pm 0.6\,\text{ppm}$

– $\eta = 0.46 \pm 0.03$

Characterization of Lanthanide oxalates by X-Ray diffraction

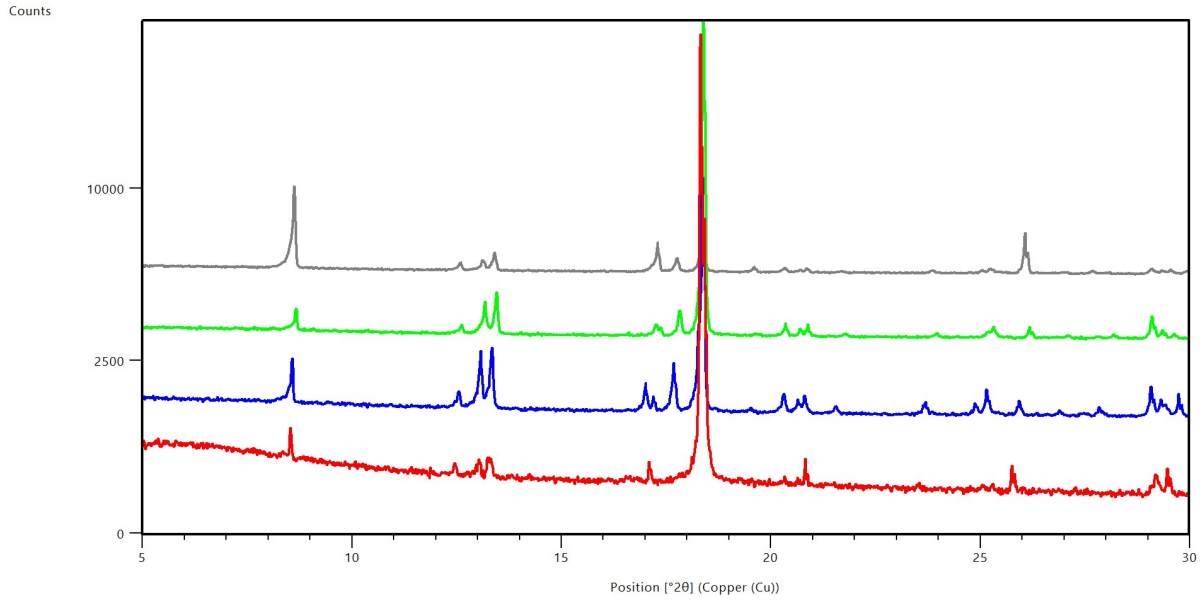

Figure S5: X-ray diffractograms of powdered lanthanide oxalates $[Ln_2(C_2O_4)_3]$, $9.5H_2O$, with, from top to bottom Ln=Pr (grey, top), Ln=Nd (green), Ln=Ce (blue) and Ln=La (red, bottom)

The isostructurality of the 3 paramagnetic phases (top) is quite obvious given the similarity of the 3 diffractograms. The lanthanum phase (bottom, red) shows the main features of its paramagnetic counterparts despite a stronger noise in the data, asserting its isostructurality with the other members of this series.

Table S1: Curie-Weiss parameters for paramagnetic lanthanide oxalates (compounds (2) to (4))

Compound	Curie constant ($Å^3$.K)	Weiss Temperature (K)
(2)	15.13	-28.3
(3)	34.71	-52.6
(4)	34.24	-46.4

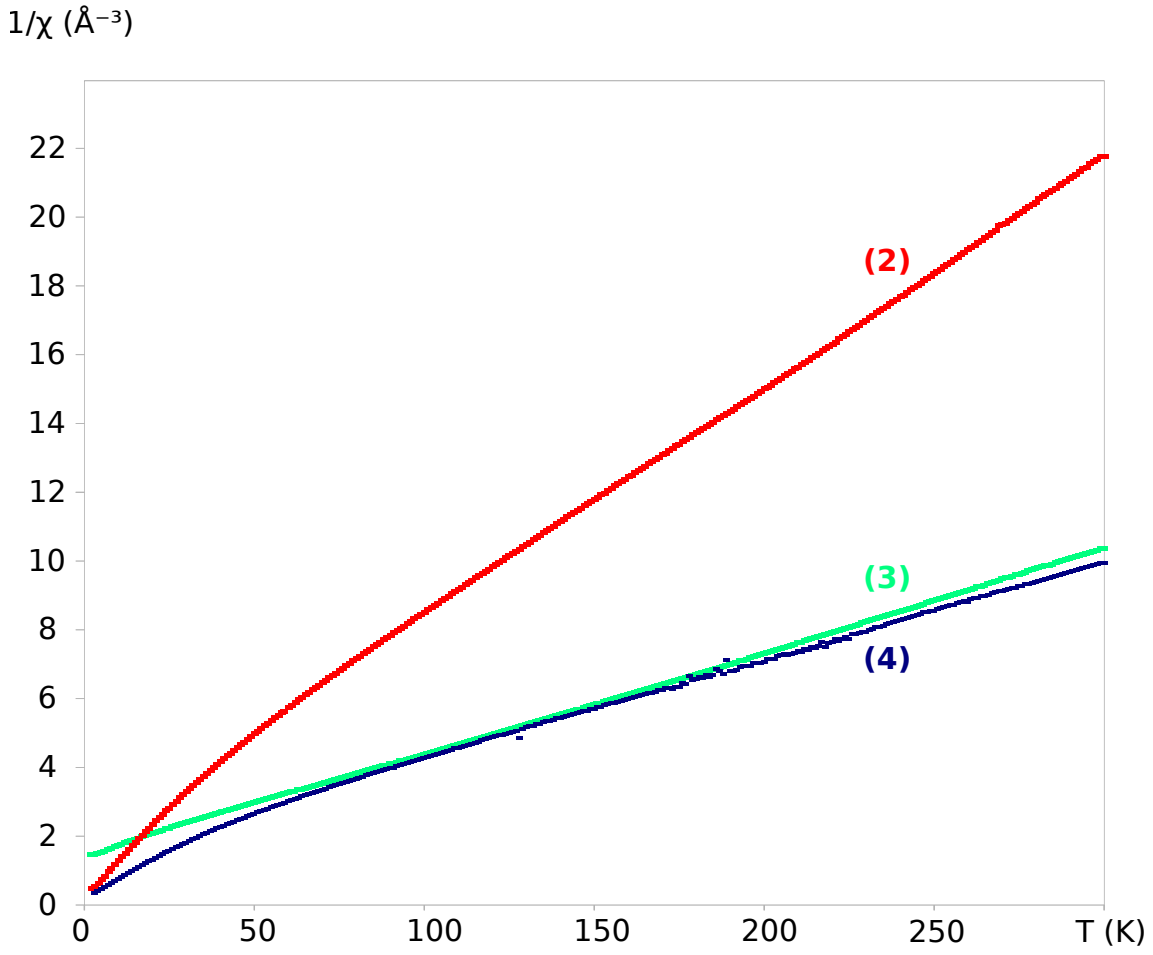

Figure S6: SQUID measured inverse isotropic magnetic susceptibility for cerium (2), praseodymium (3) and neodymium (4) oxalates. The results correspond to the value of the macroscopic measurement scaled down to one magnetic center. This data was fitted with a Curie-Weiss law based on the linear part of each curve (100-300 K)

SQUID Magnetic susceptibility measurements

The results of macroscopic magnetic susceptibility measurements were scaled down to one paramagnetic center, the inverse of the local magnetic susceptibility is presented on figure S6. We fitted the local magnetic susceptibility with a Curie-Weiss law by taking into account the linear part of the $1/\chi = f(T)$ curve (between 100 K and 300 K). The results are presented in table S1.

We used these parameters to estimate the expected value for χ_{iso} in each of our experiments and compare it with what was given by the model (table 1 in the main article). The results of both measurements are in excellent agreement.

DFT calculations for diamagnetic chemical shift tensors

Table S2: values of ^{13}C NMR parameters for the crystallographically inequivalent carbon sites of $[La_2(C_2O_4)_3]$, 9.5 H_2O crystalline phase, with respect to the cut-off energy value and k-points grid values

		σ_{iso}(ppm)			σ_{aniso}(ppm)			η		
E_{cut}	k-points	C1	C2	C3	C1	C2	C3	C1	C2	C3
900eV	$6 \times 6 \times 6$	2.07	1.66	1.09	-114.12	-112.57	-112.28	0.14	0.36	0.37
900eV	$10 \times 11 \times 11$	2.07	1.65	1.09	-114.11	-112.58	-112.28	0.14	0.36	0.37
1100 eV	$6 \times 6 \times 6$	2.05	1.64	1.07	-114.13	-112.59	-112.30	0.14	0.36	0.37

The GIPAW calculations give access to the absolute shielding tensors (σ). The diagonalization of the symmetric part of these tensors allows to determine their eigenvalues. Using the Haeberlen convention[S5], the three eigenvalues can be ordered such as $|\sigma_{zz} - \sigma_{iso}| \geq |\sigma_{xx} - \sigma_{iso}| \geq |\sigma_{yy} - \sigma_{iso}|$ and the NMR parameters can be deduced from

$$\begin{aligned} \sigma_{iso} &= \frac{1}{3}\left(\sigma_{xx} + \sigma_{yy} + \sigma_{zz}\right) \\ \sigma_{aniso} &= \sigma_{zz} - \sigma_{iso} \\ \eta &= \frac{\sigma_{yy} - \sigma_{xx}}{\sigma_{aniso}} \end{aligned}$$

Isotropic chemical shift may subsequently be evaluated using the relation $\delta_{iso} = \sigma_{ref} - \sigma_{iso}$ where σ_{ref} can be deduced from a GIPAW calculation on a reference compound.

The results given in table S2 are in full agreement with the experimental data, and the full tensor matrixes (including tensor orientation within the crystal frame) were used in the model as the diamagnetic contribution to the full chemical shift tensor.

Method for determination of optimal tensor

The algorithm for tensor determination can be found in figure S7 below.

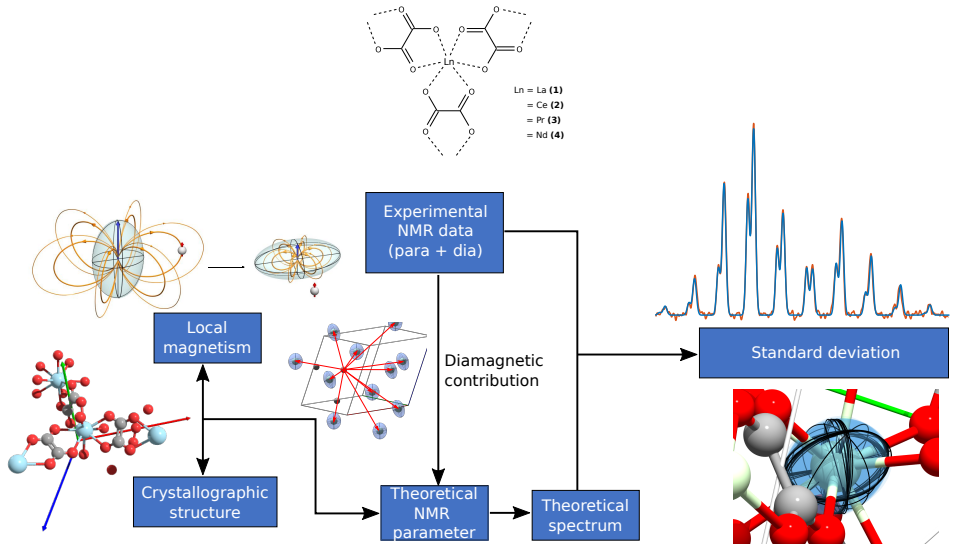

Figure S7: Procedure for local magnetism measurements: the local magnetic susceptibility tensor is parametrized and the electronic point-dipoles are generated with the crystal's symmetry operations. The paramagnetic CSA is calculated for each of the NMR-observable nucleus in the asymmetric unit and added to the diamagnetic CSA. The spectrum is generated and evaluated with respect to the experimental data in search for an optimum

This method was implemented with the Matlab(r) software and a python-based method is currently being implemented for a more general purpose and use.

The algorithm uses a module that extracts from a cif data file unit-cell parameters, symmetry operations and atomic coordinates that are then separated according to the atom type. At this point, only the coordinates of the paramagnetic centers and NMR observed

nuclei are kept.

A magnetic tensor for the paramagnetic center in the asymmetric unit is parametrized and the crystal's symmetry operations are applied in order to generate a χ tensor for each paramagnetic center in the unit-cell. Note that testing for Wickoff's position have not been implemented in this study as there was no need for it, but will be in future versions as it will be necessary to constrain the parametrization of the local χ tensor when necessary.

Once the local magnetic tensors have been set for each paramagnet in the unit-cell, a "paramagnet sphere" is generated thanks to the unit-cell vectors. This "paramagnet sphere" is an ensemble of positions and local magnetic susceptibility tensors around the NMR observed nuclei in the asymmetric unit that fall within twice the convergence radius.

From the positions of the NMR observed nuclei in the asymmetric unit and the positions and local magnetic susceptibility tensors of the paramagnetic centers in the "paramagnet sphere", the dipolar interactions between the nuclei and the average electronic moments are calculated and summed-up for each nucleus. A paramagnetic chemical shift tensor is therefore calculated and added to the diamagnetic contribution that was evaluated by DFT calculation on a diamagnetic isostructural analog, and verified by experimental CSA measurement on the same analog.

Convergence radius

The model used for this study makes calculation of NMR spectra extremely fast. However, since we generate a P1 crystal with seemingly arbitrary size, we need to give some precision about the choice of cutoff radius for nucleus-lanthanide interactions.

In order to evaluate the proper size for our simulations, we calculate the spectrum for a given crystal structure in the series of lanthanide oxalates, we give our simulation an arbitrary set of local paramagnetic tensor parameters, with a very short cutoff radius (as can be seen in figure S8). For instance, the first calculated spectrum takes into account no paramagnetic center whatsoever). Once the spectrum calculated, we normalize its integral

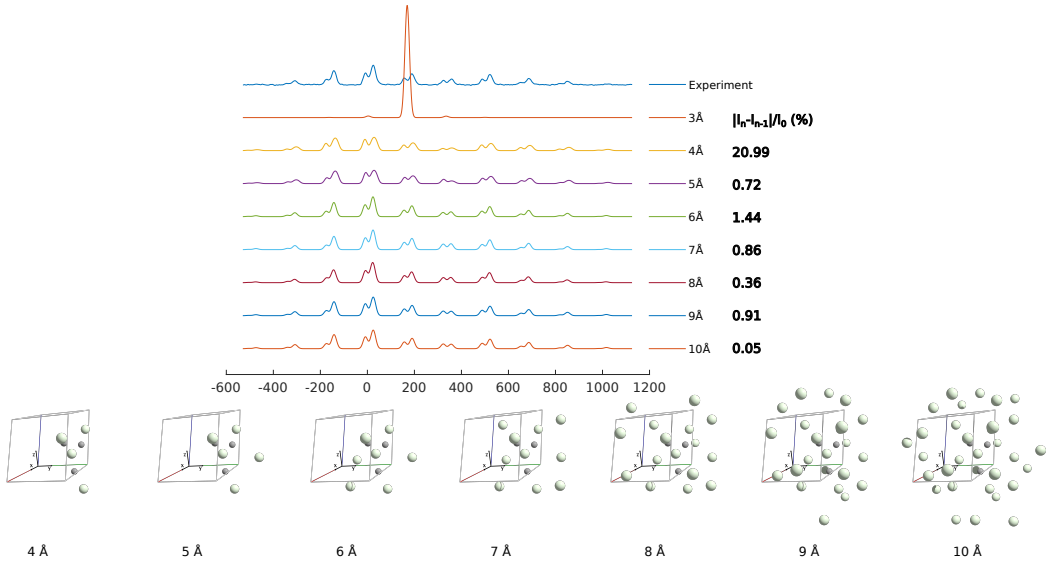

Figure S8: Illustration of calculation convergence on compound **(3)**. The paramagnetic centers taken into account for each spectrum are represented. it goes to a situation where up to 30 paramagnetic centers are necessary for convergence.

(I_0). Then we increase the cutoff radius by 1Å and perform the same calculation and the same normalization. The root-mean square difference between spectrum n and $n-1$ is integrated and divided by I_0. We estimate that our model converges when this value becomes lower that 0.1%. Once this radius is determined, since the calculation cost of this method is low, we double it for our simulations. This process is illustrated in figure S8.

Evaluation of the error on the fitting parameters

For each of the paramagnetic lanthanide oxalate in the series, we applied our algorithm to finding the optimum parameters for the local magnetic susceptibility tensor.

However, in order to evaluate the robustness of our model and the accuracy of our measurements, we reinforced our program with a Monte-Carlo-based evaluation.

After characterizing the noise in the FID, we generated a set of 500 noise-only FIDs with the same standard deviation, number of points and apodization as our experimental data. After Fourier transform of these noise-only FIDs, we repeated the fitting procedure 500 with each set of noise added to the model. The resulting fits are presented in figure S9

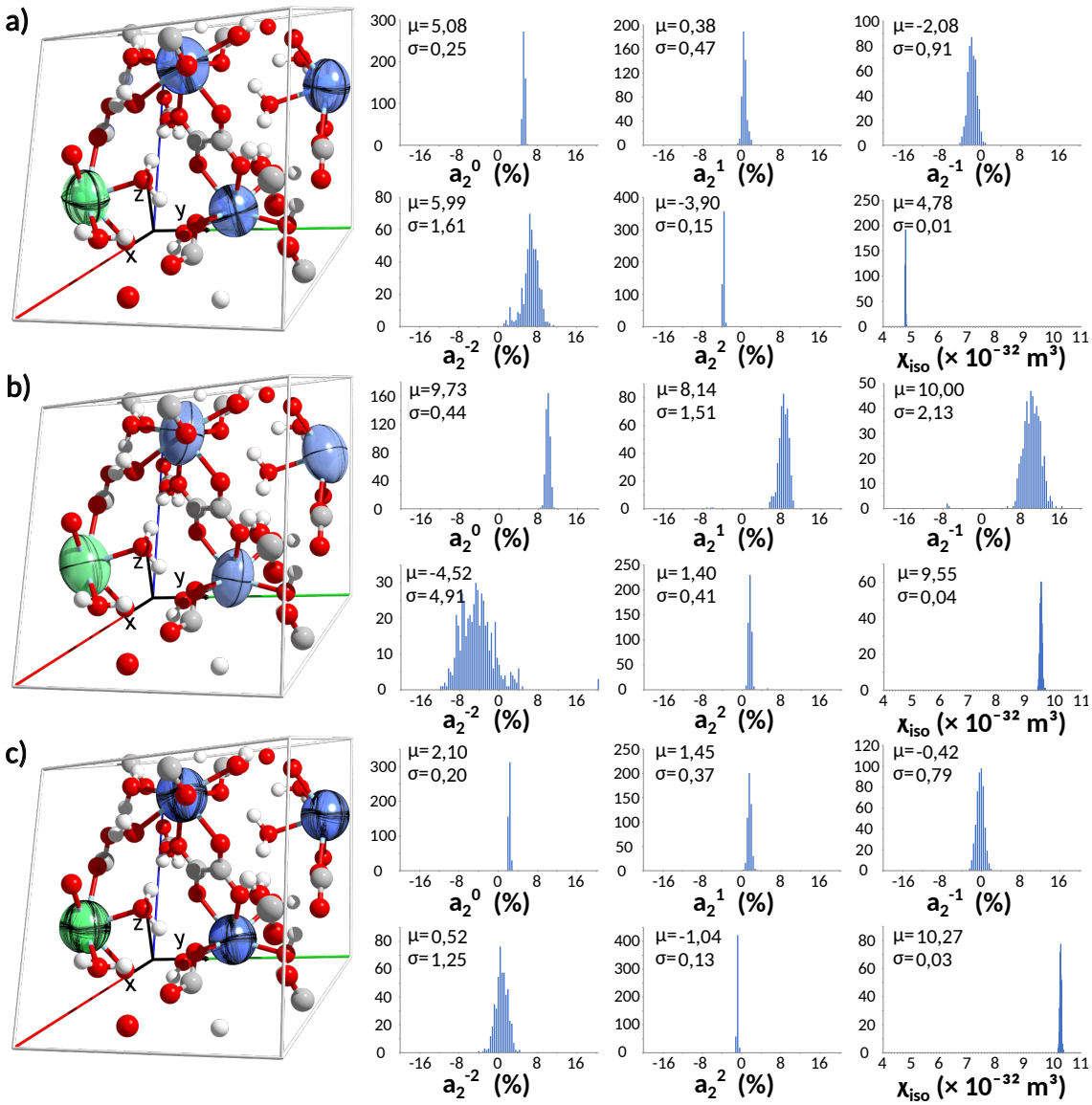

Figure S9: Error analysis for the local magnetic susceptibility tensor for: a) $[Ce_2(C_2O_4)_3]$, 9.5 H_2O, b) $[Pr_2(C_2O_4)_3]$, 9.5 H_2O and c) $[Nd_2(C_2O_4)_3]$, 9.5 H_2O. The amplitude of the spherical harmonics terms a_2^p come from equation 5 of the main text are in % of the isotropic susceptibility, which is itself in m^3 . For each parameter, the average value μ as well as the standard deviation σ are given. A subset (for readability reasons) of these results for each unit cell is represented under the shape of an ellipsoid bundle.

Euler representation of local magnetic susceptibility tensors

Here we present the results proposed in the main text of this article under a different point of view. Instead of using a deformation of the isotropic shift by rank-2 spherical harmonics, we use the more intuitive Euler representation of the local magnetic susceptibility tensor.

It is interesting to note that for cerium and praseodymium oxalates, the distribution of the isotropic value of the local magnetic susceptibility, the anisotropy of magnetic susceptibility as well as the Euler angle are very consistent. Concerning neodymium oxalate, there is still a strong consistency with the isotropic value and the anisotropy, but the Euler angles are not consistent. It is not surprising however as, with a very low δ_χ parameter, the magnetic susceptibility is almost isotropic and defining the principal axis system in such case is much more subject to measurement errors.

The asymmetry parameter however appears to be unreliable in all cases. There is an interesting parallel to be made with Hodgkinson and Emsley's paper as they also show that for the chemical shift tensor, evaluation under magic angle spinning has the lowest accuracy.

These results were used to compare the isotropic susceptibility given by our model and the susceptibility expected given the temperature in the sample (calibrated thanks to lead nitrate, vide supra).

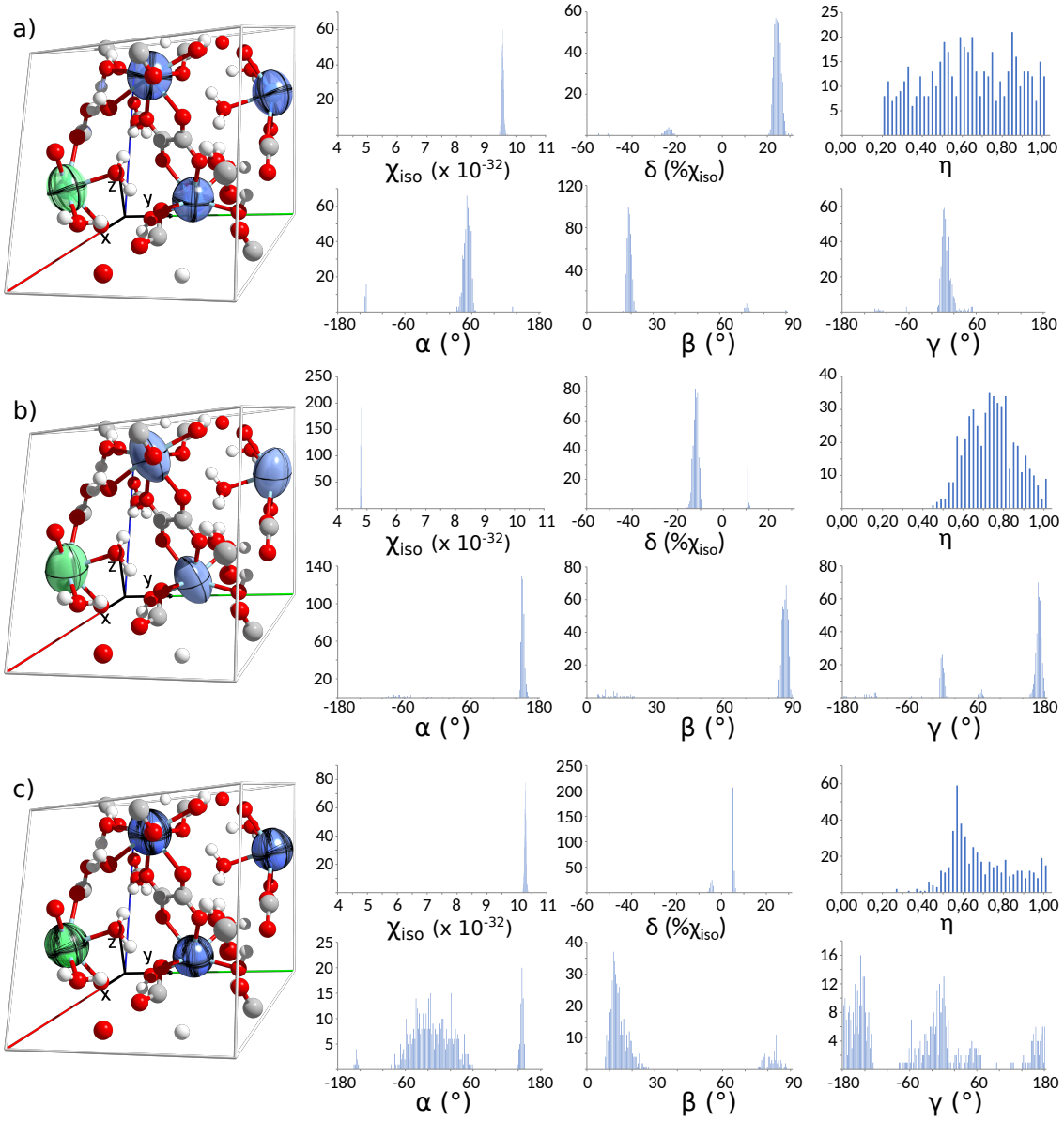

Figure S10: Error analysis for the local magnetic susceptibility tensor for: a) $[Ce_2(C_2O_4)_3]$, 9.5 H_2O, b) $[Pr_2(C_2O_4)_3]$, 9.5 H_2O and c) $[Nd_2(C_2O_4)_3]$, 9.5 H_2O. Here, the parameter basis for the local magnetic susceptibility tensor is given by the isotropic value χ_{iso} (in m^3), its principal axis system anisotropy δ (in % of χ_{iso}) and asymmetry (η, unitless), and the 3 Euler angles formed by the principal axis system with respect to the chosen frame (in °). A subset (for readability reasons) of these results for each unit cell is represented under the shape of an ellipsoid bundle.

Robustness of the model

Since the accuracy of the measure can be questioned as we can see a few percent difference in the isotropic magnetic susceptibility, and the anisotropy of magnetic susceptibility is in general in the order of several percent of the isotropic value, one can question the validity of this model. However, the NMR spectra are extremely sensitive to the anisotropy of magnetic susceptibility. If we vary the isotropic component of χ by 5%, the effects of such variation are visible, but need to be compared with a variation of the same amount on the anisotropy $\Delta\chi$. Such result is visible on figure S11.

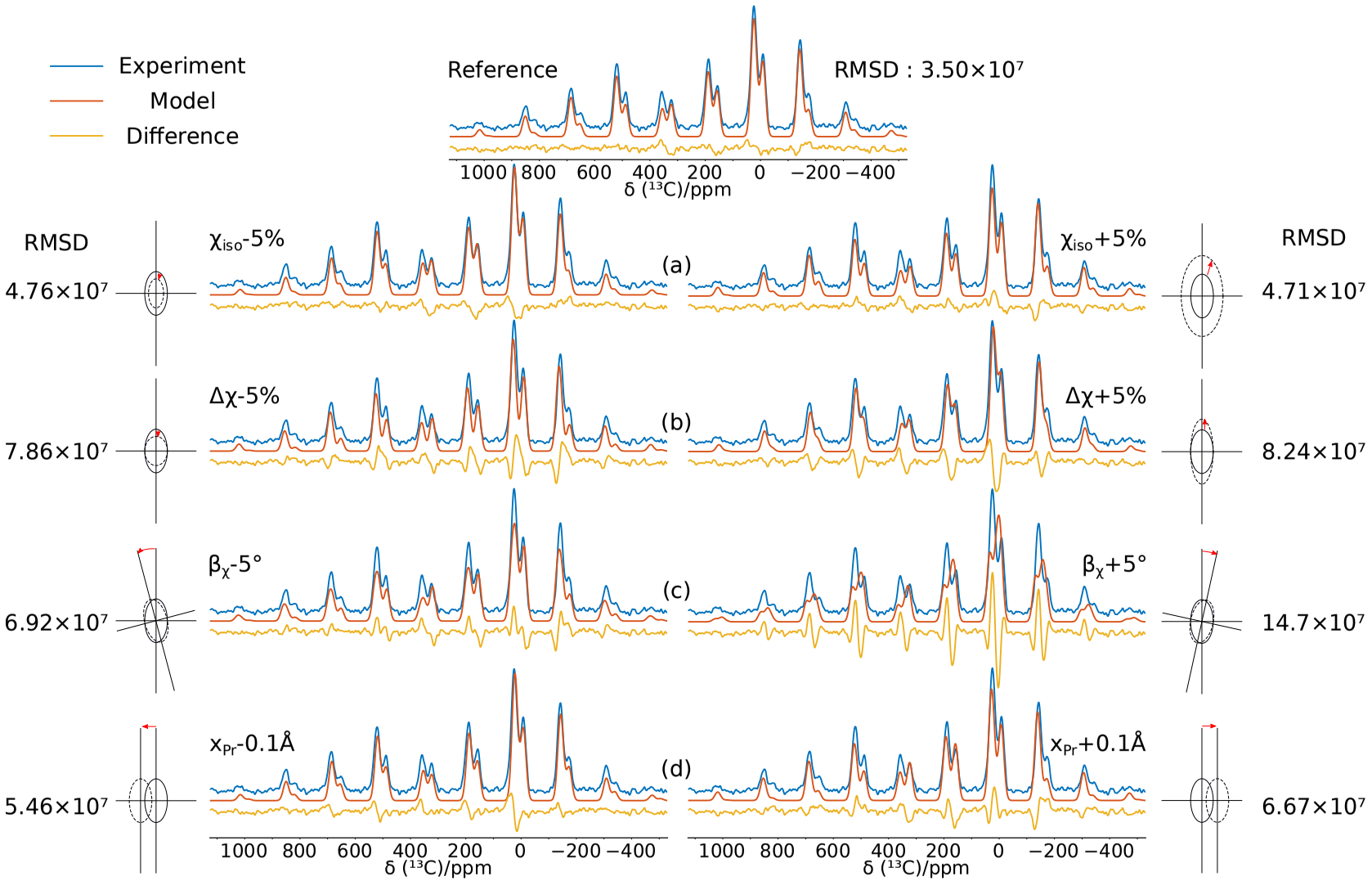

Figure S11: This figure displays several attempts at modifying the parametrization of the optimized $\mathbb{X}$ tensor for the praseodymium oxalate. The reference spectrum, model (obtained from parameter optimization with our program) and difference between the two are plotted on top, and each variation on the bottom. The RMSD between the model and the optimized spectrum shows an RMSD not different from the RMS value of experimental noise (3.54×10^7). The modification of χ_{iso} (a) deviates significantly the model-spectrum, but not quite as much as the same variation on $\Delta\chi$ along the principal axis of the tensor (b) or even worse for a modification of the direction of the principal axis of the $\mathbb{X}$ tensor itself (c). We also show that the model is sensitive to lanthanide position (d)

References

(S1) Dalal, P. V.; Saraf, K. B.; Shah, S. Growth of barium oxalate crystals in agar–agar gel and their characterization. *Cryst. Res. Technol.* **2009**, *44*, 36–42, _eprint: https://onlinelibrary.wiley.com/doi/pdf/10.1002/crat.200800221.

(S2) Guan, X.; Stark, R. E. A general protocol for temperature calibration of MAS NMR probes at arbitrary spinning speeds. *Solid State Nucl. Magn. Reson.* **2010**, *38*, 74–76.

(S3) Kervern, G.; Pintacuda, G.; Emsley, L. Fast adiabatic pulses for solid-state NMR of paramagnetic systems. *Chem. Phys. Lett.* **2007**, *435*, 157–162.

(S4) Massiot, D.; Fayon, F.; Capron, M.; King, I.; Le Calvé, S.; Alonso, B.; Durand, J.-O.; Bujoli, B.; Gan, Z.; Hoatson, G. Modelling one- and two-dimensional solid-state NMR spectra. *Magn. Reson. Chem.* **2002**, *40*, 70–76, _eprint: https://analyticalsciencejournals.onlinelibrary.wiley.com/doi/pdf/10.1002/mrc.984.

(S5) HAEBERLEN, U., Ed. *High Resolution Nmr in Solids Selective Averaging*; Academic Press, 1976; p ii.